Whistler and Broadband Electrostatic Waves in the Multiple X-line Reconnection at the Magnetopause

Zhihong Zhong[1], Daniel Bruce Graham[2], Yuri V. Khotyaintsev[2], Meng Zhou[1], Olivier Le Contel[3], Rongxin Tang[4], and Xiaohua Deng[1]

[1]Nanchang University
[2]Swedish Institute of Space Physics
[3]CNRS/Ecole Polytechnique/Sorbonne Université/Université Paris-Saclay/Obser. de Paris
[4]Nanchang University, Institute of Space Science and Technology

November 21, 2022

Abstract

We investigate whistler-mode waves and broadband electrostatic waves (EWs) within an ion diffusion region (IDR) at the magnetopause. The quasi-parallel whistlers are observed in the separatrix regions associated with the electron anisotropy or loss-cone, while the oblique whistlers, the Buneman-type waves, and the oblique EWs are observed in the center of the current sheet associated with the accelerated electron or ion beams. The whistlers are linked with Buneman-type waves by the electron Pacman distribution rather than the wave-wave process. The accelerated cold electron beams excite the Buneman-type instabilities and make the anisotropy or loss-cone of hot electrons less apparent, which led to the conversion of the whistlers from quasi-parallel to oblique. Additionally, the oblique EWs are associated with the ion beams produced by the multiple X-line reconnection. These results provide a further understanding of the relation between plasma waves and plasma kinetics in the IDR.

Whistler and Broadband Electrostatic Waves in the Multiple X-line Reconnection at the Magnetopause

Z. H. Zhong[1,2], D. B. Graham[1], Yu. V. Khotyaintsev[1], M. Zhou[2], O. Le Contel[3], R. X. Tang[2], and X. H. Deng[2]

[1]Swedish Institute of Space Physics, Uppsala, Sweden
[2]Nanchang University, Nanchang, China
[3]Laboratoire de Physique des Plasmas, CNRS/Ecole Polytechnique/Sorbonne Université/Univ. Paris Saclay/Observatoire de Paris, Paris, France

Key Points:

- Large-amplitude electromagnetic and electrostatic waves are observed in the separatrices and center of the diffusion region, respectively.
- Quasi-parallel whistlers, oblique whistlers, and Buneman-type waves are linked via the evolution of electron Pacman distribution.
- The oblique broadband electrostatic waves associated with the ion beams are observed in the diffusion region.

Corresponding author: Z. H. Zhong, zhong.zh@outlook.com

Corresponding author: M. Zhou, monmentum82@gmail.com

Abstract

We investigate whistler-mode waves and broadband electrostatic waves (EWs) within an ion diffusion region (IDR) at the magnetopause. The quasi-parallel whistlers are observed in the separatrix regions associated with the electron anisotropy or loss-cone, while the oblique whistlers, the Buneman-type waves, and the oblique EWs are observed in the center of the current sheet associated with the accelerated electron or ion beams. The whistlers are linked with Buneman-type waves by the electron Pacman distribution rather than the wave-wave process. The accelerated cold electron beams excite the Buneman-type instabilities and make the anisotropy or loss-cone of hot electrons less apparent, which led to the conversion of the whistlers from quasi-parallel to oblique. Additionally, the oblique EWs are associated with the ion beams produced by the multiple X-line reconnection. These results provide a further understanding of the relation between plasma waves and plasma kinetics in the IDR.

Plain Language Summary

The whistler waves and the broadband electrostatic waves are two common waves produced by magnetic reconnection in space plasma. Generally, the whistler waves have two modes, the quasi-parallel and the oblique to the ambient magnetic field associated with different generation mechanisms. Both of them have been observed in the magnetic reconnection, but their relation is still unclear. The broadband electrostatic waves are sometimes simultaneously observed with the oblique whistlers. The relationship between them is also inconclusive. Here, we present a new view of the relation between the quasi-parallel whistlers, the oblique whistlers, and the broadband electrostatic waves. They are linked by the evolution of electron Pacman distribution, which is composed of the hot magnetospheric population with the loss-cone and the cold accelerated magnetosheath beam characteristic for magnetopause reconnection, in the reconnection diffusion region rather than the wave-wave process. Besides, the oblique electrostatic waves associated with ion beams are observed in the diffusion region. These results advance our understanding of the relation between plasma waves and magnetic reconnection.

1 Introduction

Magnetic reconnection is a fundamental process that converts magnetic energy to plasma thermal and kinetic energy during the macroscopic changes in magnetic field topology (Biskamp, 1996). One of the important products of magnetic reconnection is plasma waves. They can efficiently produce particle heating, diffusion, and anomalous effects, which can potentially affect magnetic reconnection. In addition, plasma waves can precisely mark the deformation of electron and ion velocity distribution functions (VDFs), corresponding to the small-scale plasma kinetics in magnetic reconnection.

The whistler-mode waves are generally characterized by a high degree of polarization, positive and high ellipticity, and frequency range from $\sim 0.1 f_{ce}$ to $1 f_{ce}$ (Taubenschuss et al., 2014). Previous observations and simulations show that the whistler-mode waves exist in various regions in reconnection, such as separatrix regions (Graham, Vaivads, et al., 2016; Wilder et al., 2016, 2017; Uchino et al., 2017; Zhou et al., 2011, 2018; Khotyaintsev et al., 2020; Fujimoto & Sydora, 2008), exhausts (Le Contel et al., 2009; Khotyaintsev et al., 2011; Viberg et al., 2014; Fu et al., 2014; Wei et al., 2007; Zhou et al., 2013), diffusion regions (Tang et al., 2013; Cao et al., 2017; Wilder et al., 2019; Le Contel, Retinò, et al., 2016), and magnetic flux ropes (MFRs) (Huang et al., 2016; Jiang et al., 2019; Wang et al., 2019). Whistler waves are generated by unstable structures in the electron VDFs created by magnetic reconnection, such as loss-cones (e.g. Graham, Vaivads, et al., 2016), beams (e.g. Ren et al., 2019), perpendicular temperature anisotropies (e.g. Cao et al., 2017). They can also be excited through Cherenkov emission from electron holes (Goldman et al., 2014; Steinvall et al., 2019). Generally, whistler-mode waves generated by loss-cones, perpendicular temperature anisotropies, or electron holes have small wave normal angles, with respect to those generated by electron beams via Landau resonance (Wilder et al., 2017; Khotyaintsev et al., 2019, 2020). It was suggested that whistler waves can mediate reconnection (Deng & Matsumoto, 2001; Khotyaintsev et al., 2004; Mandt et al., 1994) and efficiently interact with electrons to provide fast pitch-angle scattering.

The broadband EWs are another type of waves that have frequently been observed in different regions of reconnection. The frequency of the broadband EWs extends from below the ion plasma frequency to the electron plasma frequency (Khotyaintsev et al., 2019). Generally, the broadband EWs have a small wavelength (on the order of several Debye lengths), and sometimes very large amplitude (above 100 mV/m). The properties (e.g. phase speed, wave potential, frequencies, propagating direction) of the broadband EWs are highly dependent on their generation mechanism (Graham et al., 2015). The beam instability (Graham et al., 2015; Graham, Khotyaintsev, et al., 2016; Liu et al., 2019; Khotyaintsev et al., 2020), Buneman instability (Khotyaintsev et al., 2010, 2016; Norgren et al., 2015), and the streaming instability (Omura et al., 1996; Ergun, Holmes, et al., 2016) are typically suggested to be responsible for the generation of these EWs in magnetic reconnection. It has been confirmed that broadband EWs can contribute to the thermalization of the plasma by wave-particle interactions in magnetic reconnection (Che et al., 2009; Khotyaintsev et al., 2020).

The broadband EWs were occasionally observed simultaneously with whistler waves during magnetic reconnection (e.g. Wilder et al., 2016, 2017; Zhou et al., 2018; Khotyaintsev et al., 2020). The relation between the two has not been fully understood yet. Here, we investigate the evolution and properties of the whistler-mode waves and broadband EWs within an ion diffusion region (IDR) at the magnetopause using the measurements from the Magnetospheric Multiscale (MMS) mission (Burch et al., 2016). These two waves overlapped with each other in some MMS observations. Different to previous studies suggesting that the EWs are excited by the nonlinear evolution of whistler waves (Drake et al., 2015; Wilder et al., 2017; Zhou et al., 2018), we show that the broadband EWs are excited through particle instabilities.

2 Event Overview

The MMS encountered the exhaust of magnetopause magnetic reconnection on 5 December 2015 when the spacecraft were located at $[9.4, -3.4, -0.7]$ R_E (Earth radius) in Geocentric Solar Magnetospheric (GSM) coordinates (Zhong et al., 2019). The MMS data used in this study are from the following instruments: the Fluxgate Magnetometer (Russell et al., 2016); the Fast Plasma Instrumen (Pollock et al., 2016); the Electric Double Probes (Lindqvist et al., 2016; Ergun, Tucker, et al., 2016); the Search Coil Magnetometer (Le Contel, Leroy, et al., 2016).

Figures 1a-1d show MMS2 observations during 00:40:00 - 00:42:20 UT in the local boundary normal (LMN) coordinates. The spacecraft were located on the magnetospheric side of the magnetopause current sheet in the southern exhaust region before 00:40:30 UT, which is characterized by the positive B_L (Figure 1b) and large ion bulk velocity in $-L$ direction, $V_{iL} \sim -400$ km/s (Figure 1d). The large $B_L \sim 50$ nT (Figure 1b), the ion temperature sharply increasing to ~ 1 keV (Figure 1a), and the density sharply decreasing to ~ 1 cm^{-3} (Figure 1c) at around 00:40:25 UT indicate that MMS detected the magnetospheric separatrix of the primary magnetopause reconnection. B_L decreases sharply and reverses sign several times during 00:40:25 - 00:42:03 UT, indicating that the spacecraft crossed the magnetopause current sheet several times in the exhaust. Finally, the spacecraft crossed the magnetosheath separatrix at around 00:42:03 UT, which is the edge of the ion outflow (Figure 1d), and moved into the magnetosheath (negative B_L and very low ion bulk velocity). There are three ion scale MFRs generated by multiple X-line reconnection in the exhaust (Zhong et al., 2019). These MFRs are manifested by the bipolar signature of B_N and the enhancements of B_M and the total magnetic field (Figure 1b). Figure 2a illustrates the MMS trajectory within the magnetopause reconnection exhaust inferred from the spacecraft observations.

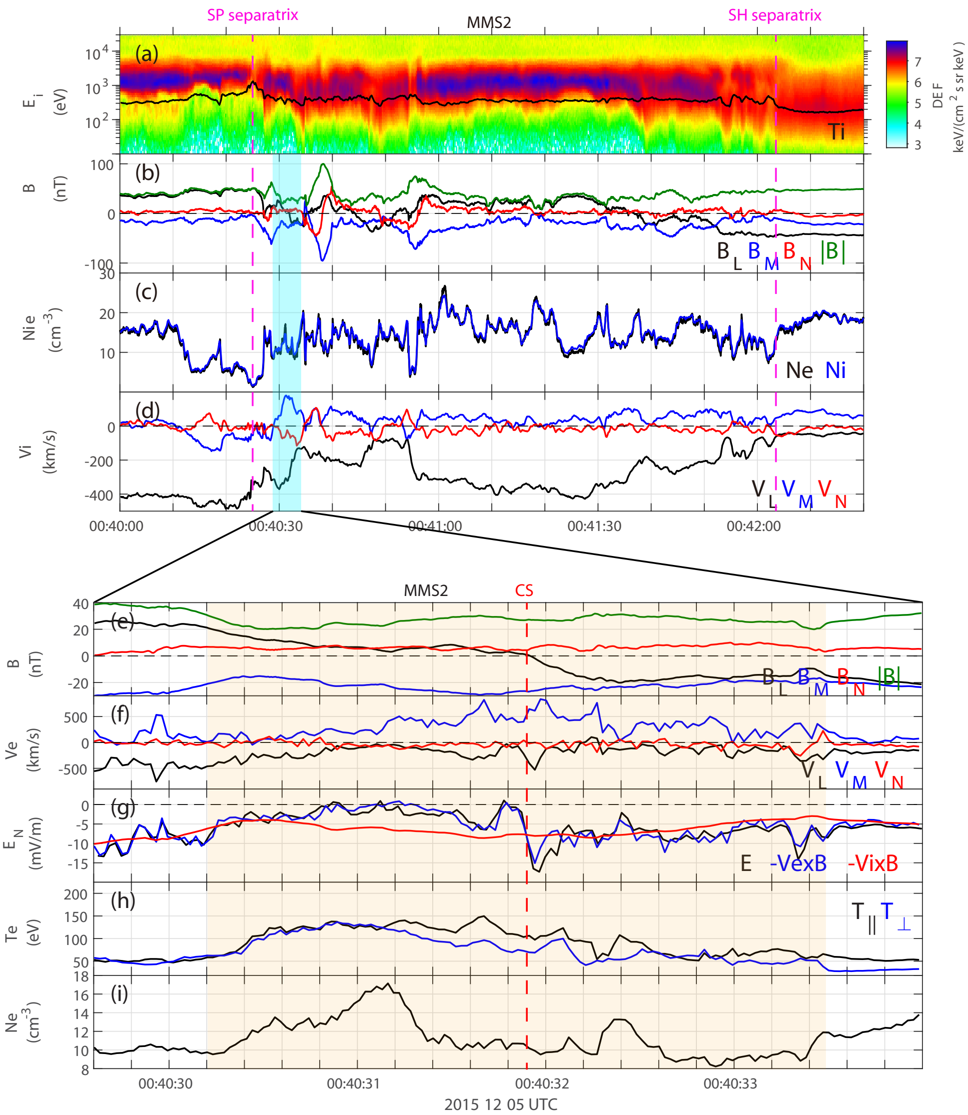

1 v3.pdf

Figure 1. Top: Overview of the southern exhaust of magnetopause reconnection observed by MMS2 on December 5, 2015. (a) ion differential energy flux and temperature (black line), (b) three components and total magnetic field, (c) electron and ion number density, (d) ion bulk velocity. Bottom: electron current sheet between the first two magnetic flux ropes. (e) three components and total magnetic field, (f) electron bulk velocity, (g) N component of the measured electric field (black), $-(V_i \times B)$(red), $-(V_e \times B)$(blue), (h) electron temperature, $T_{e\parallel}$, $T_{e\perp}$, (i) electron number density. The vector data have been transferred from GSM to LMN coordinates; $L = [0.12, -0.52, 0.85]$, $M = [-0.26, -0.84, -0.48]$, and $N = [0.96, -0.16, -0.23]$.

We focus on the region between the first two MFRs (Figure 2) where a secondary reconnecting current sheet is detected (Zhong et al., 2019). This secondary magnetic reconnection is responsible for the formation of these MFRs in the exhaust. Figures 1e-1i present the MMS2 observations during 00:40:29.60 - 00:40:34.00 UT. The current sheet crossing from the magnetospheric side to the magnetosheath side can be seen as the reversal of B_L from +20 nT to −20 nT (Figures 1e). In addition, the positive B_N (Figure 1e) and negative V_{eL} (Figure 1f) indicate that the spacecraft were located southward of the secondary reconnection site as shown in Figure 2b. A uniform $B_M \sim -20$ nT is detected throughout this interval (Figure 1e), corresponding to a guide field equal to the asymptotical magnetic field B_L.

The M component of electron bulk velocity, V_{eM}, is significantly increased in the orange shaded area (Figure 1f) with the peak value $\sim 1,000$ km/s coincident with $B_L \sim 0$. Figure 1g shows the N component of the electric field. The ion convective electric field (red curve) is different from the measured electric field (black curve), while the electron convective electric field (blue) balances the measured electric field over the orange shaded area. Furthermore, the measured electric field shows a bipolar signal from positive to negative in the ion frame consistent with variation of the Hall electric field (e.g. Zhou et al., 2016). Thus, the orange shaded area marks the IDR of the secondary magnetic reconnection. The electron temperature and density increases significantly in the IDR (Figures 1h and 1i).

3 Plasma Kinetics and Waves

Figures 3a-3f show the selected reduced two-dimensional (2D) electron VDFs, $f_e(v_\parallel, v_{E\times B})$, within the IDR from the magnetospheric side to the magnetosheath side. The evolution of the 1D electron VDFs along the magnetic field, $f_e(v_\parallel)$, are shown in Figure 3g. At the beginning of the interval, before 00:40:30.40 UT, the spacecraft are located inside the MFR where lower energy symmetric $f_e(v_\parallel)$ is observed (Figure 3g). After this, the spacecraft move into the IDR where more energetic electrons are observed. At the magnetospheric side edge of the IDR (around 00:40:30.5 UT), which is identified as the magnetospheric separatrix region of the secondary magnetic reconnection, a close to symmetric distribution is observed (Figure 3a and 3g). Figure 3a shows that the cold electron population (composed of bi-direction beams) has a parallel temperature anisotropy $T_{e\parallel} > T_{e\perp}$, while the higher energy population has a loss-cone, corresponding to a perpendicular temperature anisotropy $T_{e\perp} > T_{e\parallel}$. Figures 3b and 3c show that the cold beams are accelerated to higher energy when they get closer to the center of the current sheet. Meanwhile, the accelerated beams become weaker and the hot population becomes

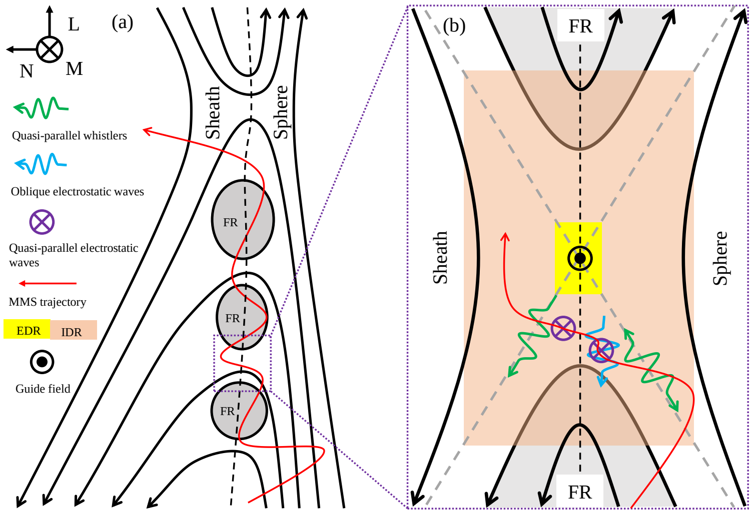

2 v3.pdf

Figure 2. (a) Sketch of MMS trajectory within the southern exhaust of magnetopause reconnection, and (b) a zoom-in view of the reconnecting current sheet located between the first two magnetic flux ropes.

more isotropic. These features indicate that the perpendicular temperature anisotropy ($T_{e\perp} > T_{e\|}$) of the hot population is subdued by the accelerated and scattered bi-direction cold beams (Figure 3c). Additionally, the Pacman distribution, which is composed of the hot magnetospheric population with the loss-cone and the cold accelerated magnetosheath beam characteristic for magnetopause reconnection, implies that the magnetic field line is opened inside the IDR (Khotyaintsev et al., 2019).

Figure 3g shows that $f_e(v_\|)$ becomes more asymmetric during the interval 00:40:31.2 - 00:40:33.5 UT corresponding to the spacecraft moving into the central region of the current sheet and the magnetosheath side of the IDR. The evolution of the Pacman distribution from the magnetosheath side to the center of the current sheet is similar to that from the magnetospheric side to the center of the current sheet. The anti-parallel cold beam originating from the magnetosheath was accelerated when it moved from the magnetosheath separatrix region (Figure 3f) to the center of the current sheet (Figures 3d and 3e). Then, the accelerated anti-parallel cold beam partially filled the anti-parallel loss-cone resulting in the loss-cone becoming less apparent at the central region of the current sheet (Figures 3d and 3e). After 00:40:33.5 UT, the spacecraft crossed the magnetosheath separatrix into the magnetosheath inflow region (Figure 2b), where $f_e(v_\|)$ becomes symmetric again (Figure 3g). It has been suggested that the Pacman distribution can be unstable to both quasi-parallel and oblique whistlers at the same time (e.g.

Khotyaintsev et al., 2019). Thus, two whistler-modes may be expected to appear in the IDR.

Figure 3h shows the evolution of 1D ion VDFs in L direction, $f_i(v_L)$. The main population consistent with the L component of the ion bulk velocity (white curve in Figure 3h) is observed throughout this interval, which is the accelerated ion outflow produced by the primary magnetopause reconnection. One can see that an additional narrow beam (~ -500 km/s, above the bulk velocity) in $-L$ direction is observed only within the IDR, especially the central region of the current sheet. It is an unmagnetized ion beam in the IDR produced by the secondary magnetic reconnection. The instabilities associated with the ion beam may appear in the IDR.

As expected, there are intense E and B fluctuations observed within the IDR. We investigate the plasma waves at frequencies above 30 Hz. Figure 3i presents the amplitude distribution of such E (black cross) and B (red circle) fluctuations related to the change of the reconnecting magnetic field B_L in time. The magnitude of B_L can mark the relative distance between the spacecraft and the magnetopause current sheet ($B_L = 0$). Figures 3j and 3k show the waveforms of E and B fluctuations at frequencies above 30 Hz, respectively. The maximum amplitude of E fluctuations is above 100 mV/m (Figure 3j), while that of B fluctuations is above 1 nT $\sim 5\%$ of the ambient magnetic field (Figure 3k). One can see that these intense E and B fluctuations are localized within the IDR associated with the unstable electron and ion VDFs. Furthermore, the large-amplitude B fluctuations are present in the separatrix regions (both magnetospheric and magnetosheath separatrix regions) far away from the central current sheet, while the large-amplitude E fluctuations are present in the regions closer to the central current sheet (Figures 2b and 3i-3k).

Figure 3l shows the power spectrum of B fluctuations for $f > 30$ Hz. They are confined to $f < 0.5 f_{ce}$ (f_{ce}, electron cyclotron frequency) and have ellipticity close to 1 (right-hand polarization close to circular, Figure 3m), indicating that the B fluctuations are whistler-mode waves. The large-amplitude whistler-mode waves are present in the magnetospheric and magnetosheath separatrix regions (Figures 2b, 3i, and 3k). Such waves have small wave-normal angles ($\theta_k < 20°$) corresponding to $\delta B_\parallel < \delta B_\perp$ (Figure 3k). We find that these whistler-mode waves are field-aligned propagating in the magnetosheath separatrix region (around 00:40:32.80 UT). Their phase velocity is $V_{ph} \sim 2,100$ km/s estimated by $|\delta E_\perp|/|\delta B_\perp|$, where $\delta E_\perp$ and $\delta B_\perp$ are the perpendicular wave electric field and magnetic field, respectively. The $n = -1$ cyclotron resonant speed of electrons (Kennel, 1966), $v_\parallel = \lambda_\parallel (f - f_{ce})$ where $\lambda_\parallel = V_{ph}/f$, is $\sim -12,000$ km/s ($f = 90$ Hz and $f_{ce} = 580$ Hz) corresponding to the hot antiparallel loss-cone in the magnetosheath separatrix region (Figure 3f). In addition, both field-aligned and anti-field-aligned propagating whistler-mode waves are observed in the magnetospheric separatrix region (around 00:40:30.60 UT) with $V_{ph} \sim 2,800$ km/s. The $n = -1$ cyclotron resonant electron speed of electrons is $\sim 13,000$ km/s ($f = 140$ Hz and $f_{ce} = 790$ Hz) corresponding to the hot perpendicular temperature anisotropy (Figures 3a and 3b). These indicate that the quasi-parallel whistler-mode waves are generated by loss-cone or perpendicular temperature anisotropy at the separatrix regions. We can see that the amplitudes of B fluctuations are decreased in the central region of the current sheet (Figure 3k). The amplitudes of the parallel component are similar to that of the perpendicular components consistent with the oblique propagation, $\theta_k \sim 50°$, Such oblique waves propagate both in the field-aligned and anti-field-aligned direction as well. The oblique whistler-mode waves can be generated by the electron beam via Landau resonance (Fujimoto, 2014; Ren et al., 2019).

Figures 3n and 3o show the power spectra of $E_{\parallel}$ and $E_{\perp}$ fluctuations for $f > 30$ Hz, respectively. The large-amplitude E fluctuations show a broadband spectra both in $E_{\parallel}$ and $E_{\perp}$ components (Figure 3n and 3o). There are two intense groups of broadband E fluctuations observed in the central region of the current sheet. Additionally, there are no corresponding B fluctuations observed, indicating broadband EWs. We focus on the first group when we start to see the ion beam signature at -500 km/s (around 00:40:31 UT). The frequencies of the maximum power of the $E_{\perp}$ component (Figure 3n) is close to ion plasma frequency (f_{pi}, blue line) and above f_{ce}, while that of the $E_{\parallel}$ component (Figure 3o) is less than f_{ce} (red line). This might imply that the broadband EWs are composed of at least two different wave modes.

Figures 4a and 4b show the waveforms of this broadband EWs (gray shaded area), which are separated into the high- and low-frequency (HF and LF, Figures 4a and 4b) components by high-pass filtering at 600 Hz and low band-pass filtering between 200 and 600 Hz, respectively. Figure 4c shows the difference between the power of $E_{\parallel}$ and $E_{\perp}$ components, $E_{\parallel}^2 - E_{\perp}^2$. It is clear that the LF waves have $E_{\parallel}^2 > E_{\perp}^2$, while the HF waves have $E_{\perp}^2 > E_{\parallel}^2$. These two modes of the broadband EWs are mixed together in the gray shaded area. We are unable to completely separate them in order to analyze their propagating direction. Fortunately, one of these two components of the broadband EWs is observed separately in the vicinity of this mixed group. The purple shaded area in Figure 4a marks the individual HF waves which are dominated by $E_{\perp}$ (Figure 4c). We found that the HF waves have $k = [-0.91, 0.38, 0.13]$ in LMN coordinates obtained by the maximum variance analysis of the wave electric field. This indicates that the HF waves are propagating in the L direction and obliques to the ambient B ($\theta_k \sim 60°$, Figure 4d) as illustrated in Figure 2b. Here, the ambient B is dominated by guide field B_M. Furthermore, the yellow shaded area in Figure 4b marks the individual LF waves which are dominated by $E_\parallel$ (Figure 4c). We found that the LF waves have $k = [-0.05, 1.00, -0.03]$ in LMN coordinates. It is propagating in the M direction and quasi-parallel to the ambient B ($\theta_k \sim 16°$, Figure 4e). The different propagation directions imply that the HF and LF waves have different generation mechanisms.

We use the 120-m separation between the spin-plane double probes for multi-probe interferometry (Graham et al., 2015; Graham, Khotyaintsev, et al., 2016) to estimate the phase velocity of the LF waves since the ambient B is close to the spacecraft spin plane during this interval. Unfortunately, the phase velocity can be determined only for the LF, but not for the HF waves since they are oblique to the ambient B. Figures 4f and 4g present the frequency-wavenumber power spectrum $P(f, k)/P_{max}$ in the gray and yellow shaded areas, respectively. They are obtained from E_{sc-p3} and E_{p4-sc} of MMS2. We see that a linear relation can be found between the frequencies of peak power and the $k_\parallel$ at LF range ($f < 800$ Hz). The $k_\parallel$ of the LF is during 0.01-0.03 m^{-1}, indicating the LF waves have wavelengths of the order of a few Debye lengths ($200 - 630$ m $\sim 10 - 32\lambda_D$, where $\lambda_D \sim 20$ m is the local Debye length given $T_e = 130$ eV and $n_e = 15$ cm^{-3}) consistent with previous studies (e.g. Graham, Khotyaintsev, et al., 2016; Khotyaintsev et al., 2016). Using linear fits to the data, we found that the wave speeds are about -178 km/s and -142 km/s for the LF waves in the gray and yellow shaded areas, respectively. They are slightly less than the local ion thermal velocity. In addition, the second broadband EWs group, which is located on the magnetosheath side (around 00:40:32.10 UT, Figure 3), shows similar properties to the LF waves. The slow speed of the LF waves suggests the Buneman-type instabilities should be the sources of the observed LF waves. The generation mechanism of the HF oblique EWs is unclear.

4 Discussion

Previous studies suggested that both the quasi-parallel and oblique whistler-mode waves can be generated at the outflow regions and separatrix regions which are far away from the IDR. A part of such whistler-mode waves can propagate toward and into the X-line (e.g. Wilder et al., 2019). In this paper, both quasi-parallel and oblique whistler-mode waves are observed in the IDR. Their evolution is consistent with the evolution of electron Pacman distributions, thus we suggest that they are generated by local unstable electron VDFs within the IDR rather than propagating from the outside. We note that the amplitudes of quasi-parallel mode are significantly larger than that of oblique mode, indicating that the quasi-parallel mode carries more energy in reconnection. Ad-

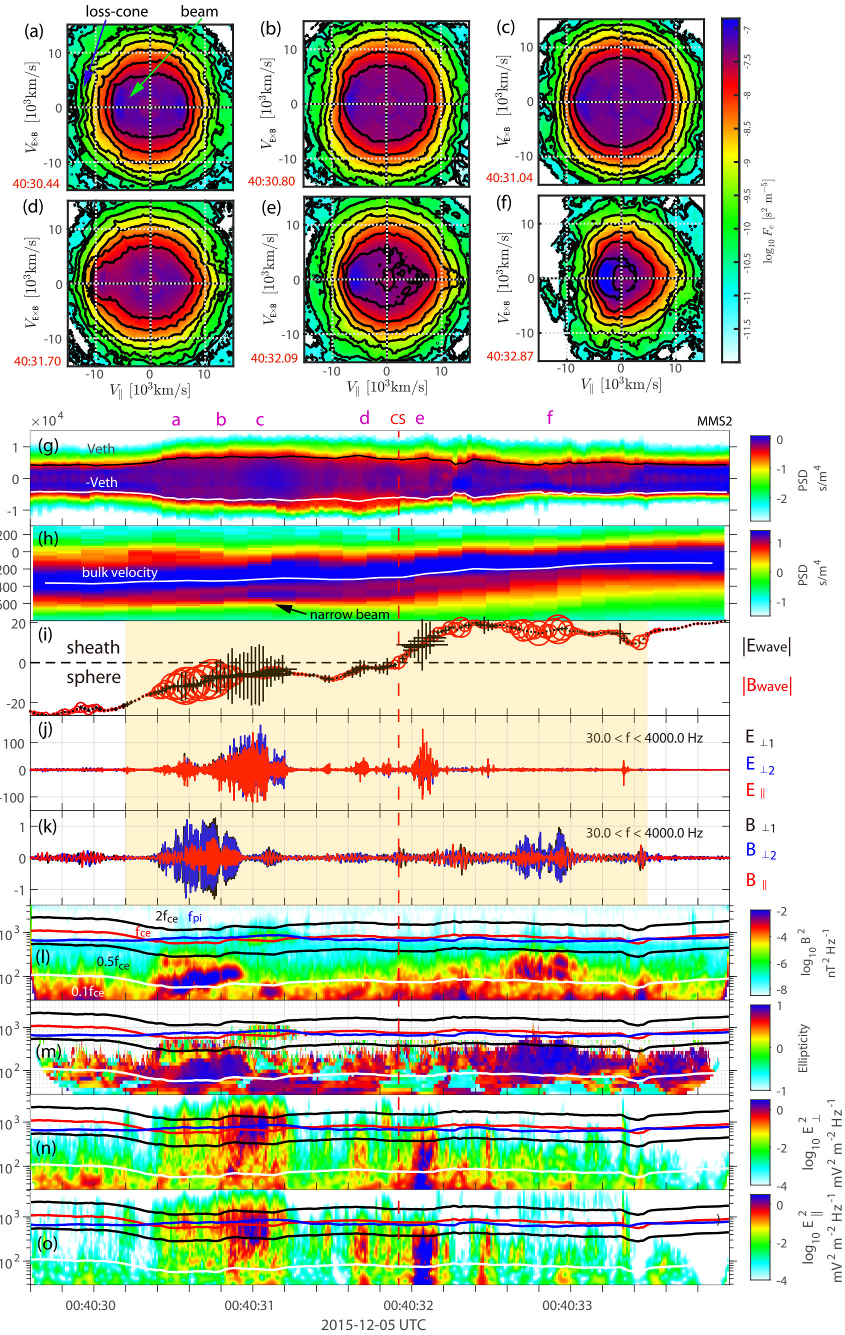

3 v3.pdf

Figure 3. Plasma waves associated with ion and electron reduced velocity distribution functions (VDFs). (a)-(f) 2-dimensional (2D) reduced electron VDFs observed at the times indicated in the panels, (g) integrated 1D electron VDFs along the magnetic field, (h) integrated 1D ion VDFs along the L direction, (i) evolution of waves related to L component of the magnetic field, (j) E and (k) B waveforms with the frequency greater than 30 Hz, (l) B spectrum and (m) ellipticity, (n) $E_\perp$ and (o) $E_\parallel$ spectra. f_{pi} and f_{ce} stand for ion-plasma and electron-cyclotron frequencies, respectively.

ditionally, the whistler-mode waves correspond to the enhancement of the electron temperature. It may contribute to the non-adiabatic heating of electrons in the IDR (Khotyaintsev et al., 2020).

For the broadband EWs, in addition to the phase velocity, the propagation direction is also highly dependent on the generation source. For example, the LF Buneman-type waves propagating in the anti-field-aligned direction ($+M$ direction in LMN coordinates) is consistent with the anti-parallel accelerated electron beams within the IDR. Although the phase velocity of the HF waves cannot be obtained, we found that the propagation direction of HF waves is close to L direction. Furthermore, we found that there are ion beams in $-L$ direction (Figure 3h), while the unstable electron distributions are observed in the M direction rather than L direction since the electrons are magnetized within the IDR due to the guide field. Considering their frequency is close to f_{pi}, we suggest that the HF waves associate with the oblique ion beams are probably oblique ion-acoustic waves, but the related ion instability is unknown. The waves associated with ion instability within the IDR have rarely been reported at present. Further studies are needed to determine whether the EWs associated with ion beams are commonly present within the IDR and their potential effects on magnetic reconnection.

It has been reported that intense broadband parallel EWs can be driven by the nonlinear evolution of anisotropy-driven whistler-mode waves (Drake et al., 2015). We found that the whistler-mode waves and broadband EWs are not linked via wave-wave processes (e.g. nonlinear steepening) in this event, but rather by the evolution of the Pacman distribution characteristic for magnetopause reconnection with significant temperature asymmetry across the magnetopause. The beams in the Pacman distributions originate from the magnetosheath rather than the scattering of nonlinear whistler-mode waves. The strength of the loss-cones and the beams vary across the IDR, generating different types of waves. Close to the magnetospheric or magnetosheath side the electron beam is weak and the loss-cone or temperature anisotropy is very pronounced, hence the quasi-parallel whistler-mode waves are generated, while closer to the central region of the current sheet the electron beam is strong and the loss-cone or temperature anisotropy is weak, and thus the dominant wave mode generated are EWs. And in the middle, we observe the mixture of the two, with the addition of beam-driven oblique whistler-mode waves.

5 Conclusions

In conclusion, we have investigated the whistler-mode waves and broadband EWs observed in an IDR. This reconnecting current sheet of the multiple X-line reconnection was observed by MMS at the magnetopause under a moderate guide field ($B_g \sim 1B_L$).

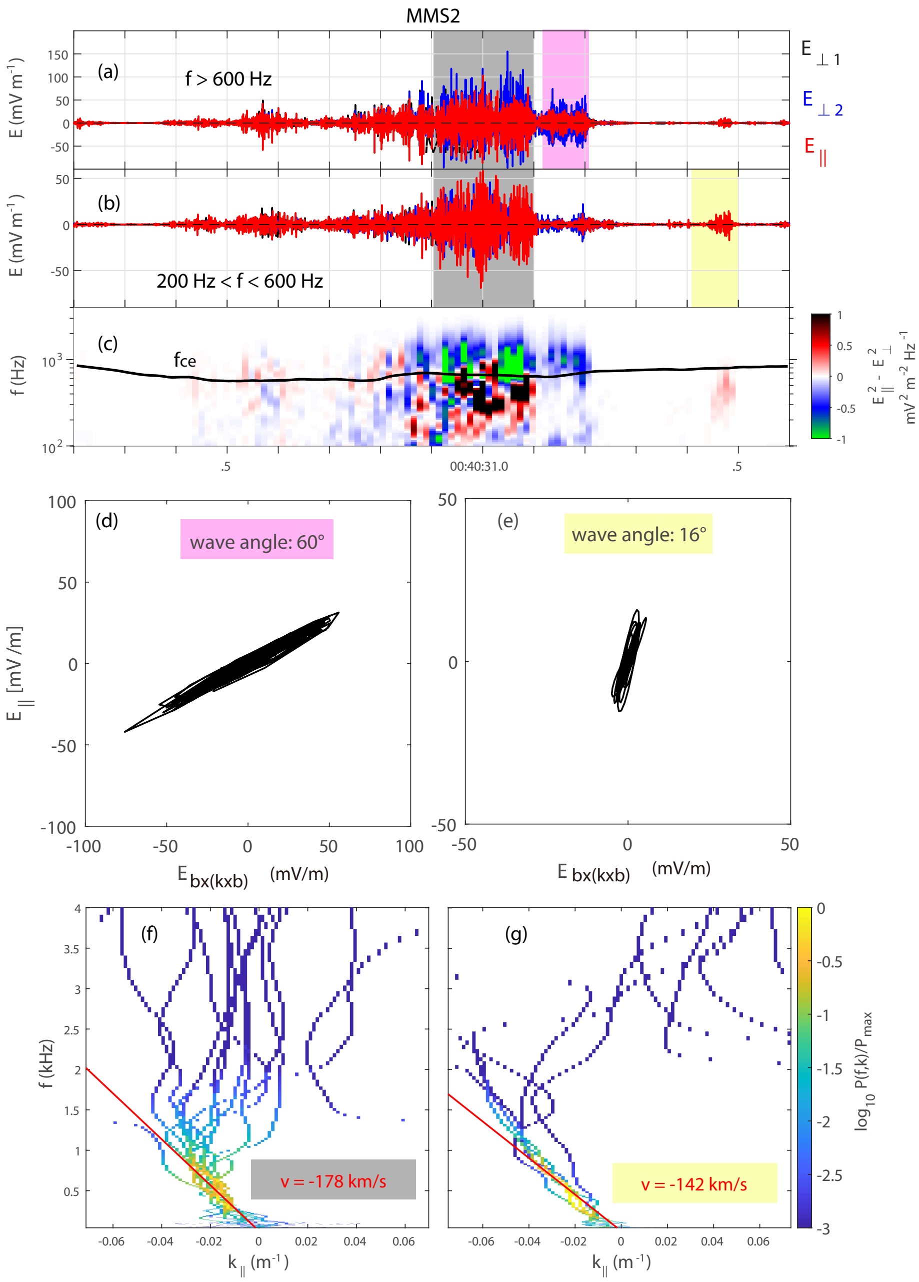

4 v3.pdf

Figure 4. Two components of broadband electrostatic waves. (a)-(b) E-HF and LF waveforms; (c) the difference between the power of parallel and perpendicular components of E fluctuations, $E_{\parallel}^2 - E_{\perp}^2$; (d) and (e) typical wave E polarization for oblique ion acoustic-like waves, sampled at 00:40:31.15 UT (purple area), and Buneman-type waves, sampled at 00:40:31.45 UT (yellow area), respectively; (f) and (g) frequency-wave number power spectra obtained from 00:40:31.00 UT (gray area) and 00:40:31.45 UT (yellow area), respectively.

The different waves are generated in different locations as illustrated in Figure 2. The key results are:

(1) The quasi-parallel whistler-mode waves are observed in the separatrix regions, while the oblique whistler-mode waves and broadband EWs are observed in the region closer to the central current sheet.

(2) The quasi-parallel whistler-mode waves are generated by the electron perpendicular temperature anisotropy or loss-cone and have large amplitude, while the oblique whistler-mode waves are driven by the electron beam and have small amplitude. The evolution of the whistler-mode waves from quasi-parallel to oblique is attributed to the evolution of the electron Pacman distribution.

(3) The whistler-mode waves and the broadband EWs are not linked by the wave-wave process in this event, but rather by the evolution of electron Pacman distribution throughout the reconnection region. The broadband EWs are composed of the Buneman-types waves and the oblique EWs associated with ion beams.

We have shown that the evolution and properties of the whistler-mode waves and the broadband EWs in the IDR reflect the localized evolution of electron and ion VDFs. Future work is needed to investigate wave generation in the diffusion region of reconnection under different ambient conditions (e.g. guide field, asymmetry, background flow).

Acknowledgments

We thank the entire MMS team and MMS Science Data Center for providing the high-quality data for this study. The French LPP involvement for the SCM instrument was supported by CNES and CNRS. This work was supported by National Natural Science Foundation of China (NSFC) under grants No. 41674144, No. 41774154, No. 41974195, and No. 42074197; the Swedish National Space Board, grant 128/17; the Swedish Research Council, grant 2016-05507; and the Interdisciplinary Innovation Fund of Natural Science from Nanchang University under grant 9166-27060003-YB14. The spacecraft data used for this study are publicly available from the MMS Science Data Center: `https://lasp.colorado.edu/mms/sdc/public/`.

References

Biskamp, D. (1996). Magnetic reconnection in plasmas. *Astrophysics and Space Science*, *242*(1-2), 165–207.

Burch, J., Moore, T., Torbert, R., & Giles, B. (2016). Magnetospheric multiscale overview and science objectives. *Space Science Reviews*, *199*(1-4), 5–21.

Cao, D., Fu, H., Cao, J., Wang, T., Graham, D. B., Chen, Z., ... others (2017). Mms observations of whistler waves in electron diffusion region. *Geophysical Research Letters*, *44*(9), 3954–3962.

Che, H., Drake, J., Swisdak, M., & Yoon, P. (2009). Nonlinear development of streaming instabilities in strongly magnetized plasma. *Physical review letters*, *102*(14), 145004.

Deng, X., & Matsumoto, H. (2001). Rapid magnetic reconnection in the earth's magnetosphere mediated by whistler waves. *Nature*, *410*(6828), 557–560.

Drake, J., Agapitov, O., & Mozer, F. (2015). The development of a bursty precipitation front with intense localized parallel electric fields driven by whistler waves. *Geophysical Research Letters*, *42*(8), 2563–2570.

Ergun, R., Holmes, J., Goodrich, K., Wilder, F., Stawarz, J., Eriksson, S., ... others (2016). Magnetospheric multiscale observations of large-amplitude, parallel, electrostatic waves associated with magnetic reconnection at the magnetopause. *Geophysical Research Letters*, *43*(11), 5626–5634.

Ergun, R., Tucker, S., Westfall, J., Goodrich, K., Malaspina, D., Summers, D., ... others (2016). The axial double probe and fields signal processing for the mms mission. *Space Science Reviews*, *199*(1-4), 167–188.

Fu, H., Cao, J., Cully, C., Khotyaintsev, Y. V., Vaivads, A., Angelopoulos, V., ... others (2014). Whistler-mode waves inside flux pileup region: Structured or unstructured? *Journal of Geophysical Research: Space Physics*, *119*(11), 9089–9100.

Fujimoto, K. (2014). Wave activities in separatrix regions of magnetic reconnection. *Geophysical Research Letters*, *41*(8), 2721–2728.

Fujimoto, K., & Sydora, R. D. (2008). Whistler waves associated with magnetic reconnection. *Geophysical research letters*, *35*(19).

Goldman, M., Newman, D., Lapenta, G., Andersson, L., Gosling, J., Eriksson, S., ... Ergun, R. (2014). Čerenkov emission of quasiparallel whistlers by fast electron phase-space holes during magnetic reconnection. *Physical review letters*, *112*(14), 145002.

Graham, D. B., Khotyaintsev, Y. V., Vaivads, A., & André, M. (2015). Electrostatic solitary waves with distinct speeds associated with asymmetric reconnection. *Geophysical Research Letters*, *42*(2), 215–224.

Graham, D. B., Khotyaintsev, Y. V., Vaivads, A., & Andre, M. (2016). Electrostatic solitary waves and electrostatic waves at the magnetopause. *Journal of Geophysical Research: Space Physics*, *121*(4), 3069–3092.

Graham, D. B., Vaivads, A., Khotyaintsev, Y. V., & Andre, M. (2016). Whistler emission in the separatrix regions of asymmetric magnetic reconnection. *Journal of Geophysical Research: Space Physics*, *121*(3), 1934–1954.

Huang, S., Sahraoui, F., Retino, A., Le Contel, O., Yuan, Z., Chasapis, A., ... others (2016). Mms observations of ion-scale magnetic island in the magnetosheath turbulent plasma. *Geophysical Research Letters*, *43*(15), 7850–7858.

Jiang, K., Huang, S., Yuan, Z., Yu, X., Liu, S., Deng, D., & He, L. (2019). Observations of whistler waves in two sequential flux ropes at the magnetopause. *Astrophysics and Space Science*, *364*(10), 168.

Kennel, C. (1966). Low-frequency whistler mode. *The Physics of Fluids*, *9*(11), 2190–2202.

Khotyaintsev, Y. V., Cully, C., Vaivads, A., André, M., & Owen, C. (2011). Plasma jet braking: Energy dissipation and nonadiabatic electrons. *Physical Review Letters*, *106*(16), 165001.

Khotyaintsev, Y. V., Graham, D., Norgren, C., Eriksson, E., Li, W., Johlander, A., ... others (2016). Electron jet of asymmetric reconnection. *Geophysical Research Letters*, *43*(11), 5571–5580.

Khotyaintsev, Y. V., Graham, D. B., Norgren, C., & Vaivads, A. (2019). Collisionless magnetic reconnection and waves: progress review. *Frontiers in Astronomy and Space Sciences*, *6*.

Khotyaintsev, Y. V., Graham, D. B., Steinvall, K., Alm, L., Vaivads, A., Johlander, A., ... others (2020). Electron heating by debye-scale turbulence in guide-field reconnection. *Physical Review Letters*, *124*(4), 045101.

Khotyaintsev, Y. V., Vaivads, A., André, M., Fujimoto, M., Retinò, A., & Owen, C. (2010). Observations of slow electron holes at a magnetic reconnection site. *Physical Review Letters*, *105*(16), 165002.

Khotyaintsev, Y. V., Vaivads, A., Ogawa, Y., Popielawska, B., André, M., Buchert, S., ... Reme, H. (2004). Cluster observations of high-frequency waves in the exterior cusp. In *Annales geophysicae* (Vol. 22, pp. 2403–2411).

Le Contel, O., Leroy, P., Roux, A., Coillot, C., Alison, D., Bouabdellah, A., ... others (2016). The search-coil magnetometer for mms. *Space Science Reviews*, *199*(1-4), 257–282.

Le Contel, O., Retinò, A., Breuillard, H., Mirioni, L., Robert, P., Chasapis, A., ... others (2016). Whistler mode waves and hall fields detected by mms during a dayside magnetopause crossing. *Geophysical Research Letters*, *43*(12), 5943–5952.

Le Contel, O., Roux, A., Jacquey, C., Robert, P., Berthomier, M., Chust, T., ... others (2009). Quasi-parallel whistler mode waves observed by themis during near-earth dipolarizations. In *Annales geophysicae: atmospheres, hydrospheres and space sciences* (Vol. 27, p. 2259).

Lindqvist, P.-A., Olsson, G., Torbert, R., King, B., Granoff, M., Rau, D., … others (2016). The spin-plane double probe electric field instrument for mms. *Space Science Reviews*, *199*(1-4), 137–165.

Liu, C., Vaivads, A., Graham, D. B., Khotyaintsev, Y. V., Fu, H., Johlander, A., … Giles, B. (2019). Ion-beam-driven intense electrostatic solitary waves in reconnection jet. *Geophysical Research Letters*, *46*(22), 12702–12710.

Mandt, M., Denton, R., & Drake, J. (1994). Transition to whistler mediated magnetic reconnection. *Geophysical Research Letters*, *21*(1), 73–76.

Norgren, C., André, M., Graham, D., Khotyaintsev, Y. V., & Vaivads, A. (2015). Slow electron holes in multicomponent plasmas. *Geophysical Research Letters*, *42*(18), 7264–7272.

Omura, Y., Matsumoto, H., Miyake, T., & Kojima, H. (1996). Electron beam instabilities as generation mechanism of electrostatic solitary waves in the magnetotail. *Journal of Geophysical Research: Space Physics*, *101*(A2), 2685–2697.

Pollock, C., Moore, T., Jacques, A., Burch, J., Gliese, U., Saito, Y., … others (2016). Fast plasma investigation for magnetospheric multiscale. *Space Science Reviews*, *199*(1-4), 331–406.

Ren, Y., Dai, L., Li, W., Tao, X., Wang, C., Tang, B., … others (2019). Whistler waves driven by field-aligned streaming electrons in the near-earth magnetotail reconnection. *Geophysical Research Letters*, *46*(10), 5045–5054.

Russell, C., Anderson, B., Baumjohann, W., Bromund, K., Dearborn, D., Fischer, D., … others (2016). The magnetospheric multiscale magnetometers. *Space Science Reviews*, *199*(1-4), 189–256.

Steinvall, K., Khotyaintsev, Y. V., Graham, D. B., Vaivads, A., Contel, O. L., & Russell, C. T. (2019, 12). Observations of electromagnetic electron holes and evidence of cherenkov whistler emission. *Physical Review Letters*, *123*, 255101. doi: 10.1103/PhysRevLett.123.255101

Tang, X., Cattell, C., Dombeck, J., Dai, L., Wilson, L. B., Breneman, A., & Hupach, A. (2013, 6). Themis observations of the magnetopause electron diffusion region: Large amplitude waves and heated electrons. *Geophysical Research Letters*, *40*, 2884-2890. doi: 10.1002/grl.50565

Taubenschuss, U., Khotyaintsev, Y. V., Santolík, O., Vaivads, A., Cully, C. M., Contel, O. L., & Angelopoulos, V. (2014, 12). Wave normal angles of whistler mode chorus rising and falling tones. *Journal of Geophysical Re-*

search: Space Physics, *119*, 9567-9578. doi: 10.1002/2014JA020575@10.1002/(ISSN)2169-9402.PLASMAS

Uchino, H., Kurita, S., Harada, Y., Machida, S., & Angelopoulos, V. (2017, 3). Waves in the innermost open boundary layer formed by dayside magnetopause reconnection. *Journal of Geophysical Research: Space Physics*, *122*, 3291-3307. doi: 10.1002/2016JA023300

Viberg, H., Khotyaintsev, Y. V., Vaivads, A., André, M., Fu, H. S., & Cornilleau-Wehrlin, N. (2014, 4). Whistler mode waves at magnetotail dipolarization fronts. *Journal of Geophysical Research: Space Physics*, *119*, 2605-2611. doi: 10.1002/2014JA019892

Wang, S., Wang, R., Yao, S. T., Lu, Q., Russell, C. T., & Wang, S. (2019, 3). Anisotropic electron distributions and whistler waves in a series of the flux transfer events at the magnetopause. *Journal of Geophysical Research: Space Physics*, *124*, 1753-1769. doi: 10.1029/2018JA026417

Wei, X., Cao, J., Zhou, G., Santolík, O., Rème, H., Dandouras, I., … Fazakerley, A. (2007). Cluster observations of waves in the whistler frequency range associated with magnetic reconnection in the earth's magnetotail. *Journal of Geophysical Research: Space Physics*, *112*(A10).

Wilder, F. D., Ergun, R. E., Goodrich, K. A., Goldman, M. V., Newman, D. L., Malaspina, D. M., … Holmes, J. C. (2016, 6). Observations of whistler mode waves with nonlinear parallel electric fields near the dayside magnetic reconnection separatrix by the magnetospheric multiscale mission. *Geophysical Research Letters*, *43*, 5909-5917. doi: 10.1002/2016GL069473

Wilder, F. D., Ergun, R. E., Hoilijoki, S., Webster, J., Argall, M. R., Ahmadi, N., … Giles, B. L. (2019, 10). A survey of plasma waves appearing near dayside magnetopause electron diffusion region events. *Journal of Geophysical Research: Space Physics*, *124*, 7837-7849. doi: 10.1029/2019JA027060

Wilder, F. D., Ergun, R. E., Newman, D. L., Goodrich, K. A., Trattner, K. J., Goldman, M. V., … Lindqvist, P.-A. (2017, 5). The nonlinear behavior of whistler waves at the reconnecting dayside magnetopause as observed by the magnetospheric multiscale mission: A case study. *Journal of Geophysical Research: Space Physics*, *122*, 5487-5501. doi: 10.1002/2017JA024062

Zhong, Z. H., Zhou, M., Huang, S. Y., Tang, R. X., Deng, X. H., Pang, Y., & Chen, H. T. (2019, 6). Observations of a kinetic-scale magnetic hole in a reconnection diffusion region. *Geophysical Research Letters*, *46*, 6248-6257. doi: 10.1029/2019GL082637

Zhou, M., Ashour-Abdalla, M., Berchem, J., Walker, R. J., Liang, H., El-Alaoui, M.,

... Chandler, M. O. (2016, 5). Observation of high-frequency electrostatic waves in the vicinity of the reconnection ion diffusion region by the spacecraft of the magnetospheric multiscale (mms) mission. *Geophysical Research Letters*, *43*, 4808-4815. doi: 10.1002/2016GL069010

Zhou, M., Berchem, J., Walker, R. J., El-Alaoui, M., Goldstein, M. L., Lapenta, G., ... Marklund, G. (2018, 3). Magnetospheric multiscale observations of an ion diffusion region with large guide field at the magnetopause: Current system, electron heating, and plasma waves. *Journal of Geophysical Research: Space Physics*, *123*, 1834-1852. doi: 10.1002/2017JA024517

Zhou, M., Deng, X., Ashour-Abdalla, M., Walker, R., Pang, Y., Tang, C., ... Li, H. (2013). Cluster observations of kinetic structures and electron acceleration within a dynamic plasma bubble. *Journal of Geophysical Research: Space Physics*, *118*(2), 674–684.

Zhou, M., Pang, Y., Deng, X. H., Yuan, Z. G., & Huang, S. Y. (2011, 6). Density cavity in magnetic reconnection diffusion region in the presence of guide field. *Journal of Geophysical Research: Space Physics*, *116*, n/a-n/a. doi: 10.1029/2010JA016324

Figure 1.

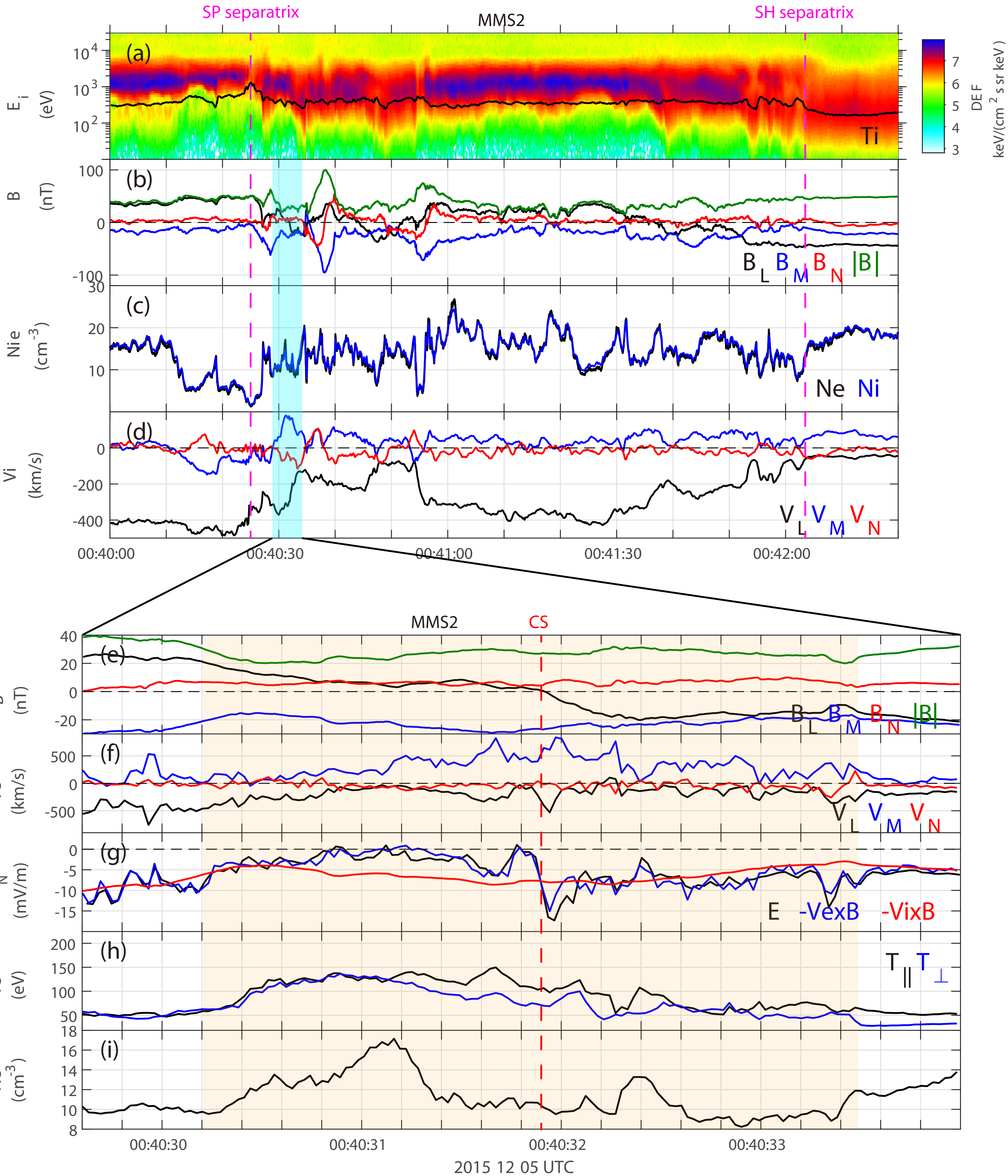

SP separatrix
MMS2
SH separatrix
(a)
Ti
(b)
B_L B_M B_N |B|
(c)
Ne Ni
(d)
V_L V_M V_N
00:40:00
00:40:30
00:41:00
00:41:30
00:42:00
MMS2
CS
(e)
(f)
(g)
E -VexB -VixB
(h)
$T_{\parallel}$ $T_{\perp}$
(i)
00:40:30
00:40:31
00:40:32
00:40:33
2015 12 05 UTC

Figure 2.

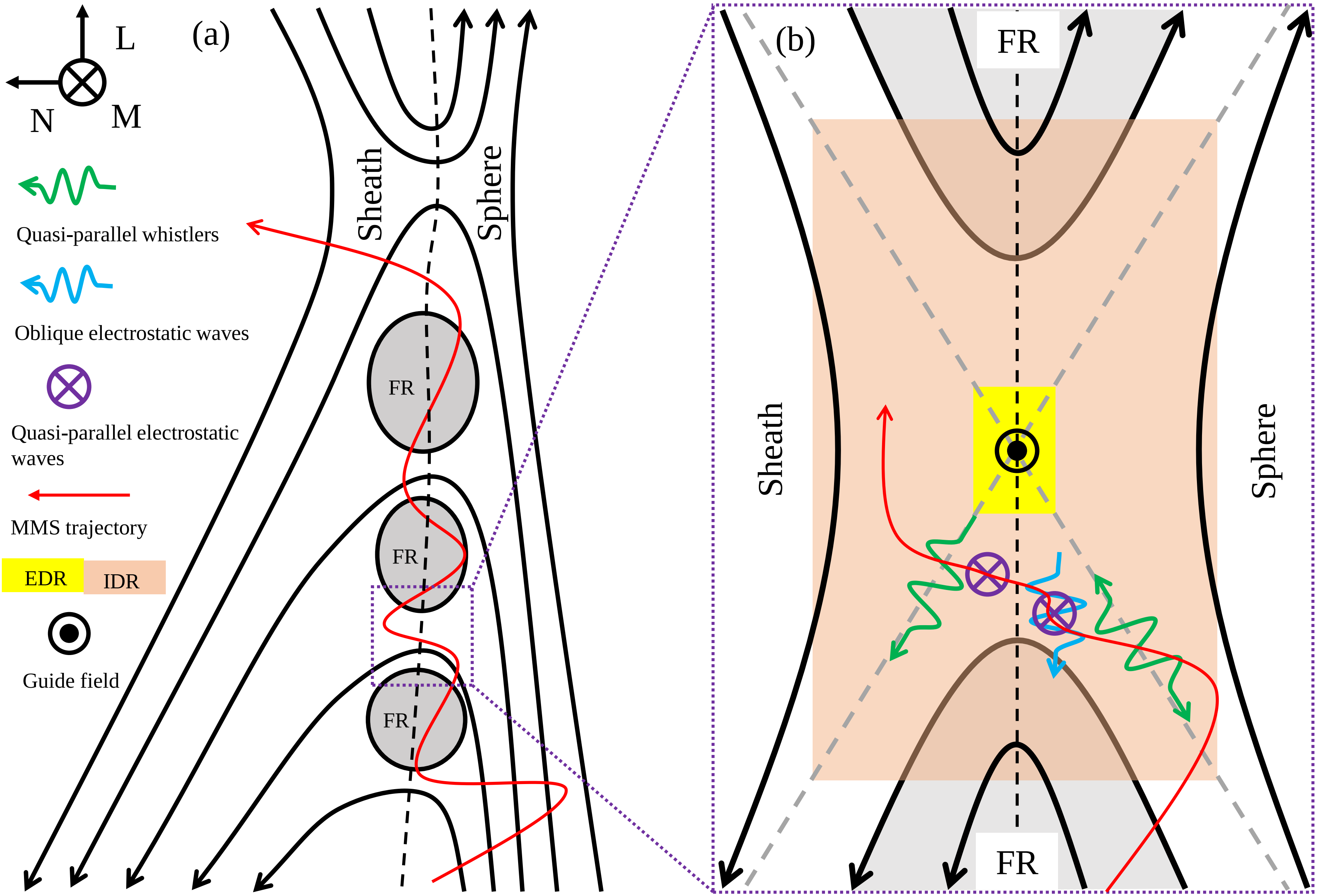

L
N
M
(a)
Quasi-parallel whistlers
Oblique electrostatic waves
Quasi-parallel electrostatic waves
MMS trajectory
EDR
IDR
Guide field
Sheath
Sphere
FR
FR
FR
(b)
FR
FR
Sheath
Sphere

Figure 3.

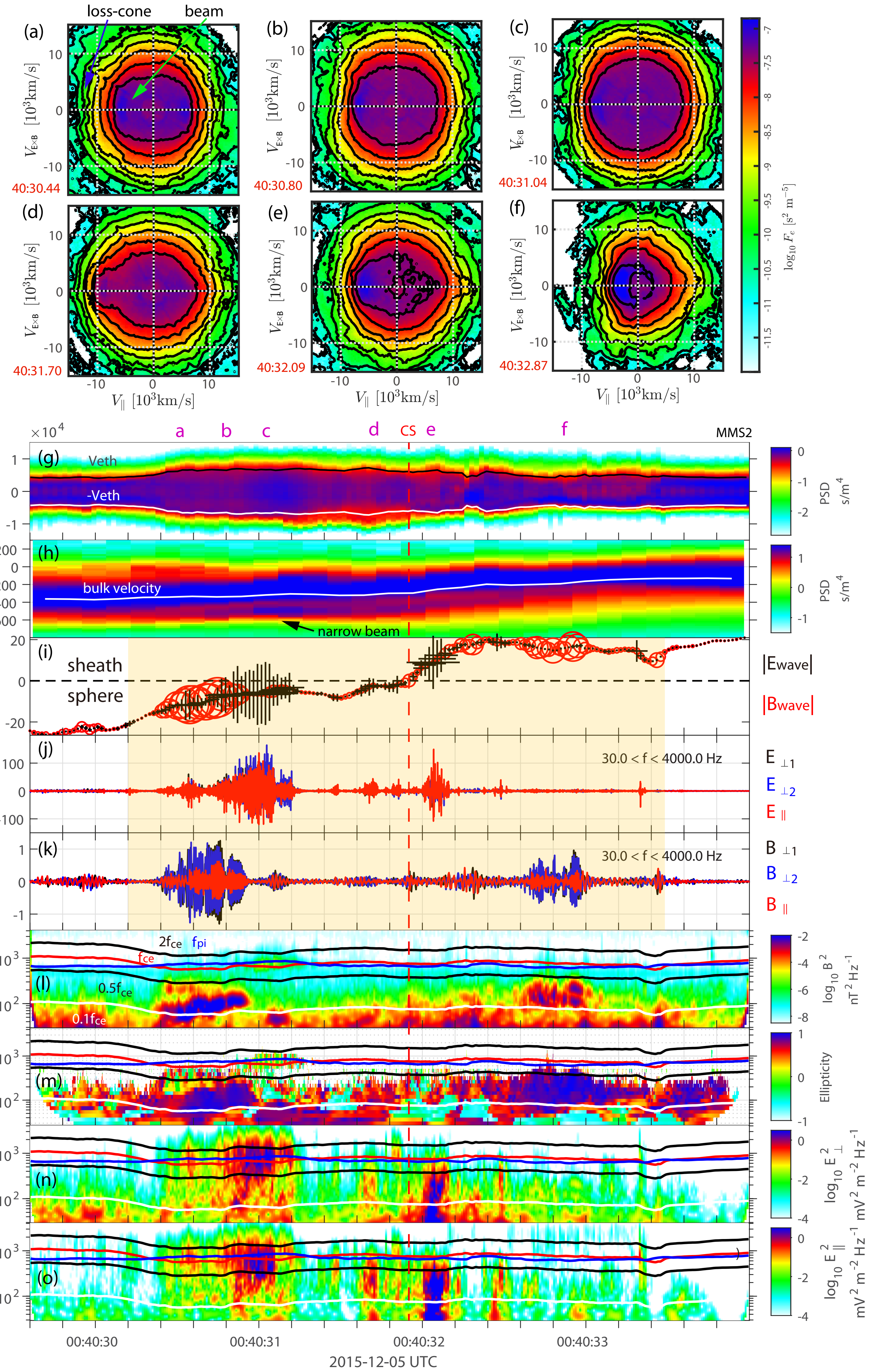

loss-cone
beam
(a)
(b)
(c)
(d)
(e)
(f)
40:30.44
40:30.80
40:31.04
40:31.70
40:32.09
40:32.87
$V_{E\times B}$ [10^3km/s]
$V_\parallel$ [10^3km/s]
$\log_{10} F_e$ [s^2 m^{-5}]
a b c d CS e f
MMS2
(g) Veth -Veth
Ve|| (km/s)
PSD s/m^4
(h) bulk velocity narrow beam
ViL (km/s)
(i) sheath sphere
-BL (nT)
|Ewave|
|Bwave|
(j) 30.0 < f < 4000.0 Hz
δ E (mV/m)
$E_{\perp1}$
$E_{\perp2}$
$E_\parallel$
(k) 30.0 < f < 4000.0 Hz
δ B (nT)
$B_{\perp1}$
$B_{\perp2}$
$B_\parallel$
(l) 2fce fpi fce 0.5fce 0.1fce
f (Hz)
$\log_{10} B^2$ nT^2 Hz^{-1}
(m)
Ellipticity
(n)
$\log_{10} E_\perp^2$ mV^2 m^{-2} Hz^{-1}
(o)
$\log_{10} E_\parallel^2$ mV^2 m^{-2} Hz^{-1}
00:40:30
00:40:31
00:40:32
00:40:33
2015-12-05 UTC

Figure 4.

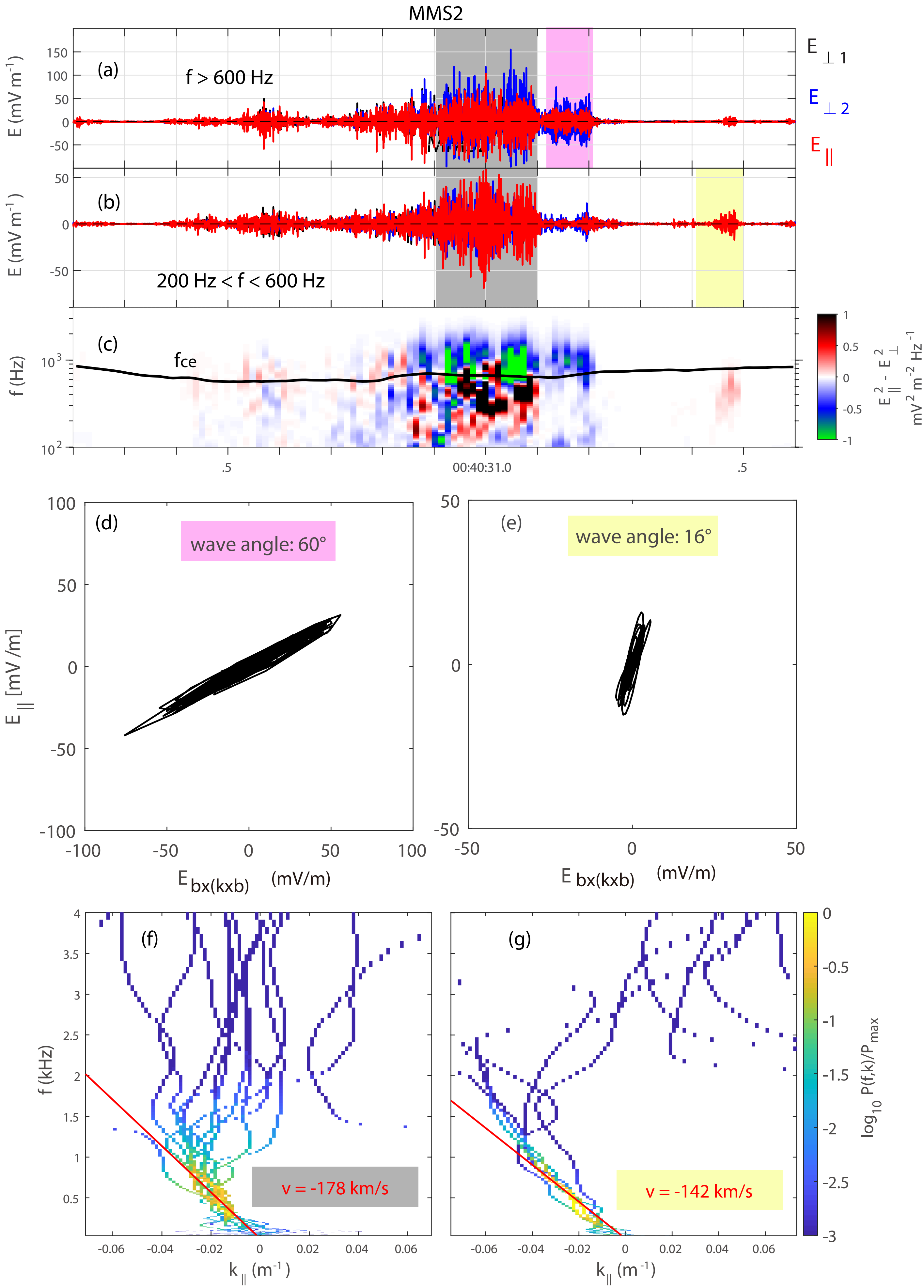
MMS2
(a)
f > 600 Hz
E ⊥1
E ⊥2
E ||
E (mV m-1)
(b)
200 Hz < f < 600 Hz
E (mV m-1)
(c)
fce
f (Hz)
E||2 - E⊥2
mV2 m-2 Hz-1
00:40:31.0
(d)
wave angle: 60°
E|| [mV /m]
Ebx(kxb) (mV/m)
(e)
wave angle: 16°
E bx(kxb) (mV/m)
(f)
v = -178 km/s
f (kHz)
k|| (m-1)
(g)
v = -142 km/s
k|| (m-1)
log10 P(f,k)/Pmax